Journal of Catalysis 273 (2010) 83–91

Contents lists available at ScienceDirect

Journal of Catalysis

journal homepage: www.elsevier.com/locate/jcat

Mechanism for CO oxidation catalyzed by Pd-substituted $BaCeO_3$, and the local structure of the active sites

Xiaoying Ouyang [a], Susannah L. Scott [a,b,*]

[a] Department of Chemistry and Biochemistry, University of California, Santa Barbara, CA 93106, USA
[b] Department of Chemical Engineering University of California, Santa Barbara, CA 93106, USA

ARTICLE INFO

Article history:
Received 27 January 2010
Revised 4 April 2010
Accepted 24 April 2010
Available online 11 June 2010

Keywords:
Perovskite
Palladium
CO oxidation
Kinetics and mechanisms
X-ray absorption spectroscopy

ABSTRACT

Ba(Ce,Pd)O_3 perovskite is an unusual catalyst for CO oxidation by O_2, given its low surface area. The rate law for the catalytic reaction was evaluated under CO-lean and CO-rich conditions, as well as near-stoichiometric conditions. When O_2 is present in excess, the kinetics show CO inhibition, consistent with a Langmuir–Hinshelwood mechanism in which both reactants compete for the same adsorption sites. The Arrhenius activation energy for this mechanism is surprisingly low, (7.8 ± 0.3) kcal/mol. It is attributed to weak adsorption of CO on ionic surface Pd(II) sites. When O_2 is limiting, the reaction orders for both CO and O_2 show a strong dependence on $P(CO)/P(O_2)$, and eventually become independent of both $P(CO)$ and $P(O_2)$ at high $P(CO)$. This suggests a new $BaCeO_3$-mediated mechanism which dominates the reaction at high $P(CO)/P(O_2)$. Its Arrhenius activation energy is (9.7 ± 0.3) kcal/mol, probably reflecting the barrier to oxygen migration in the oxide phase. Both mechanisms contribute significantly for $P(CO)/P(O_2) \approx 1$. The catalytic activity of Pd-substituted $BaCeO_3$ is attributed to the increased bulk oxygen mobility in the presence of square-planar Pd(II) ions that are located on the perovskite *B*-sites, each adjacent to an oxygen vacancy.

1. Introduction

CeO_2 has been a major component of automotive exhaust emissions catalysts since the early 1980s [1]. Both CeO_2 and its mixed oxides, such as CeO_2–ZrO_2, are well known for their oxygen storage capacity (OSC) [1–5] and dynamic oxygen exchange capacity (OEC) [3,6–10]. The $Ce^{4+/3+}$ redox couple allows these materials to store and release oxygen under fuel-lean and fuel-rich conditions, respectively. There are many synthetic routes to CeO_2-based oxides, including sol–gel methods [11,12], coprecipitation [13,14], flame synthesis [6,15,16], solid-state reactions [17,18], and electrosynthesis [19,20]. Noble metals are readily dispersed on their surfaces, promoting catalytic activity at the metal–support interface [21–26]. Oxidation of CO [27–31] and soot [32–34] can occur via a "CeO_2-mediated mechanism", making use of lattice oxygen rather than adsorbed $O_{2(g)}$.

Preventing thermal deactivation in emissions catalysts remains a challenge [35]. The temperature of the exhaust gases can rise transiently to ca. 1000 °C, while the exhaust gas fluctuates between oxidizing and reducing compositions. Under these conditions, catalysts composed of highly dispersed noble metals on CeO_2-based supports are gradually deactivated by phase transitions, loss of surface area in the support, and sintering of the metal particles [1,36,37]. Redispersion of the noble metal is required to regenerate a sintered catalyst, but successful *in situ* examples are limited. For example, 2 wt.% Pt on a Ce–Zr–Y mixed oxide underwent redistribution of large Pt particles to smaller particles in response to redox changes [38]. It was also reported that La(Co,Fe)O_3 perovskites doped with noble metals can generate and regenerate highly dispersed noble metal nanoparticles by cyclic ingress and egress of the metal during redox cycling [39].

Mixing CeO_2 with other oxides, such as in CeO_2–La_2O_3 [40], CeO_2–Y_2O_3 [41], CeO_2–Al_2O_3 [42], and CeO_2–SiO_2 [43], can increase its thermal stability, however, these materials still lose surface area over time at 1000 °C. Since CeO_2 itself also shows poor resistance to sulfur poisoning [44,45], BaO may be added in the role of SO_x absorber [46]. In addition, BaO is used in automotive emissions catalysts for NO_x storage [47,48] and to reduce washcoat (Al_2O_3) sintering [49]. The properties of the stable perovskite $BaCeO_3$ as a catalyst support and promoter of noble metal catalysis are therefore relevant. Doped barium cerate, $BaCe_{1-x}M_xO_{3-\delta}$ (M = Gd, Y, In, etc.), has found widespread use as proton conductor in solid-oxide fuel cells, where conduction is attributed to the presence of hydroxyl groups in the oxygen sublattice [50–52]. The low-temperature combustion and high-temperature oxidative dehydrogenation of ethane are catalyzed by doped $Ba(Ce_{1-x}M_x)O_{3-\delta}$ and $(Ba_{1-y}M_y)CeO_{3-\delta}$ (M = Ca, La, Y, Nd), where enhanced activity was attributed to the increased efficiency of oxygen transport [53].

* Corresponding author at: Department of Chemical Engineering, University of California, Santa Barbara, CA 93106, USA. Fax: +1 805 893 4731.
E-mail address: sscott@engineering.ucsb.edu (S.L. Scott).

0021-9517/$ - see front matter © 2010 Elsevier Inc. All rights reserved.
doi:10.1016/j.jcat.2010.04.020

Pd-containing catalysts have been widely studied for treating cold-start emissions, because of their high activity at low temperature. Recently, we showed that $BaCeO_3$ can accommodate low levels of Pd(II) on the perovskite's *B*-sites [54,55]. Since the solid-state synthesis is conducted at 1000 °C, its B.E.T. surface area is very low (ca. 1 m^2/g). However, Pd-substituted $BaCeO_3$ and highly dispersed Pd/γ-Al_2O_3 with comparable total masses of Pd have very similar light-off temperatures, T_{50}, for CO oxidation under lean conditions [55]. Furthermore, the perovskite allows Pd to move out of and back into the oxide lattice in response to reducing or oxidizing conditions, respectively. The complete reversibility of this migration was demonstrated by X-ray diffraction (XRD), neutron diffraction, and X-ray photoelectron spectroscopy (XPS) [54,55]. The thermodynamic stability of $BaCeO_3$ enables the catalyst to recover its activity fully even after exposure to temperature extremes.

In this contribution, we evaluate the rate laws for CO oxidation under a range of reaction conditions (lean, rich, near-stoichiometric) over Ba(Ce,Pd)O_3. Due to the crystalline nature of the $BaCeO_3$ host, the local environment of Pd(II) is highly uniform. Using X-ray absorption spectroscopy (XAS), we determine the coordination of the Pd(II) sites and the location of their accompanying oxygen vacancies, thereby linking catalytic activity with the structure of the noble metal sites.

2. Experimental

2.1. Materials

The solid-state synthesis of $BaCe_{1-x}Pd_xO_{3-x}$ (ρ = 6.27 g/cm^3 for x = 0.10) in flowing O_2 at 1000 °C was described previously [54]. With an aqueous solution of $Pd(NO_3)_2$ (99.5% purity, Aldrich), 2.0 wt.% PdO/γ-Al_2O_3 was prepared by incipient wetness impregnation of γ-Al_2O_3 (HTA 102; 78 m^2/g), followed by calcination in air at 600 °C for 4 h.

CO oxidation under lean conditions was performed using a premixed feed containing 1000 ppm CO and 10% O_2, balanced by argon. The calibration gas was a premixed cylinder of 1000 ppm CO_2 in N_2 (Praxair). CO oxidation under rich conditions was performed by mixing CO and O_2 (both 99.99%, Praxair) with Ar (99.999%, Praxair) in the desired ratios. The CO stream was further purified by passage through a coil of Teflon tubing immersed in a liquid nitrogen cold trap, to remove traces of metal carbonyls and residual CO_2.

2.2. Differential kinetics

Kinetics measurements were made in a Hiden CATLAB fixed-bed tubular quartz microreactor (18.50 × 0.48 cm i.d.) located in a tubular furnace with temperature control between ambient temperature and 1100 °C. The catalyst (5–20 mg) and inert BN (Aldrich) were sieved separately to either 30–60 mesh (0.25–0.60 mm) or 80–100 mesh (0.15–0.18 mm), then mixed in a 1:3 w/w ratio, and loaded into the reactor to give a bed length of ca. 1.0 cm, held in place with plugs of quartz wool. The temperature was monitored by a K-type thermocouple touching the catalyst bed. The reactant gas composition was controlled by varying the flow rates of CO, O_2, and Ar, while the total flow rate remained constant at 50 mL/min. The amount of catalyst in the reactor was chosen so that the reaction conditions were always differential, with conversions usually well below 1% of the limiting reagent. The operating pressure was 1 atm, and the pressure drop (<0.03 atm) was neglected.

Product compositions were monitored with an online quadrupole mass spectrometer (HR-20, Hiden Analytical). The electron energy and emission current were set to 70.0 eV and 250 μA, respectively. A secondary electron multiplier (SEM) detector was used to monitor the MS signal at m/z = 44 (CO_2^+), 32 (O_2^+) and 28 (CO^+). The outlet concentration of CO_2 (ppm) was calculated from the signal at m/z = 44, using a premixed calibration gas containing 1000 ppm CO_2 balanced by N_2. Similarly, the outlet concentration of O_2 was calculated from the signal at m/z = 32, using a premixed calibration gas containing 4780 ppm O_2 balanced by Ar. Since CO and CO_2 have a common ion at m/z = 28 (CO^+), the CO signal was corrected for the contribution from the ionization of CO_2. The outlet concentration of CO was calculated from the remaining signal at m/z = 28, using a premixed calibration gas containing 1050 ppm CO balanced by He.

Prior to measuring rates, each catalyst sample was exposed to a standard pretreatment involving flowing 1000 ppm CO/10% O_2 at 423 K for 1 h to ensure complete incorporation of Pd into the perovskite host as Pd(II). After the feed gas composition was changed and the MS signal had been stable for at least 20 min, the conversion X was calculated from the inlet and outlet concentrations of the limiting reagent, assuming 100% mass balance. Reaction rates were obtained from measured values of X, according to the equation $rate = X \cdot F/W$, where F is the molar flow rate of CO (mol/s) and W is the catalyst weight (g). Turnover frequencies (TOF) were calculated by estimating the number of surface Pd(II) sites; for details see Supplementary material. The uncertainties in the activation energies were estimated using error propagation, Eq. (1) [56]:

$$\left(\frac{\sigma_{E_a}}{E_a}\right)^2 = \frac{2T^2}{(\Delta T)^2}\left(\frac{\sigma_T}{T}\right)^2 + 2\left(\frac{1}{\Delta(\ln k)}\right)^2\left(\frac{\sigma_k}{k}\right)^2 \quad (1)$$

where σ_{E_a} is the calculated uncertainty in the activation energy; σ_T and σ_k are the measurement errors in the temperatures T and the rate constants k, respectively, and ΔT and $\Delta(\ln k)$ are the ranges of temperature and $\ln k$ used in the Arrhenius plot.

2.3. X-ray absorption spectroscopy

$BaCe_{0.93}Pd_{0.07}O_{2.93}$ powder (ca. 200 mg) was packed in air into a slotted polycarbonate sample holder (slot size 24 × 8 × 0.8 mm), without dilution. The slot was sealed on each side with Kapton film (0.50 mm, Chemplex). The X-ray absorption experiment was performed at the Pd *K*-edge (24,350 keV) on beamline BL2-3 (Bend) at the Stanford Synchrotron Radiation Lightsource (SSRL). X-rays were monochromatized via reflection from a pair of Si(220) crystals, φ = 90°, through a 2 × 12-mm entrance slit.

The beam was detuned by 25% to remove higher harmonics. Its intensity was measured with a N_2-filled ionization chamber. Transmitted X-rays were detected in a second, Ar-filled ionization chamber, then passed through a Pd foil (for energy calibration) into a third, Ar-filled ionization chamber. Fluorescence from the sample was recorded simultaneously using a germanium 13-element detector equipped with a Soller slit. The spectrum was recorded using a 0.35 eV step size in the pre-edge region and up to 30 eV after the edge. In the post-edge (EXAFS) region, a step size of 0.05 $Å^{-1}$ was used in order to generate equally spaced data points in *k*-space. The spectrum was acquired in six scans over 3 h at room temperature. Serially acquired spectra were compared and found to be identical in initial and subsequent sweeps, verifying that no sample decomposition occurred during data collection.

Data were acquired using the SSRL MicroEXAFS Data Collector 1.0. Data processing, analysis, and plotting were carried out using IFEFFIT 1.2.10 [57]. The EXAFS spectrum was generated from the average of six ASCII files. The spectrum was background-corrected and normalized by first subtracting a linear fit to the pre-edge region extrapolated the length of the entire spectrum, then dividing by a third-degree polynomial fitted to the post-edge region. The

$\chi(k)$ data were k^3-weighted and fitted by a polynomial spline with six knots between 2.0 and 16.0 $Å^{-1}$. This k-weighting was chosen because it generates a uniform χ amplitude across the range of usable data [58]. Subtraction of the spline decreases contributions from low-frequency atomic X-ray absorption fine structure (AXAFS) [59]. A Bessel window was applied to the data range before Fourier-transformation to R-space.

Curve fitting was performed in R-space on the k^3-weighted data. FEFF6 was used to calculate theoretical values for the bond distances R, based on the computed structure. Refinements were performed by non-linear least-squares fitting of the structural parameters R_i and σ_i^2, using Artemis [60]. Coordination numbers (N) were held fixed at integer values. The energy shift (ΔE_0) was constrained to be the same for all scatterers. The amplitude reduction factor (S_0^2) was obtained by curve fitting the EXAFS of *fcc*-Pd to its published crystal structure [61] and was then fixed as a global parameter.

3. Results and discussion

3.1. CO oxidation activity of the crystalline perovskite catalyst

The extremely low surface area of Pd-substituted $BaCeO_3$ (ca. 1 m^2/g) is, surprisingly, not incompatible with high activity for CO oxidation. Previously, we reported that $BaCe_{0.9}Pd_{0.1}O_{2.9}$ (3.3 wt.% Pd) and a conventional high surface area Pd/γ-Al_2O_3 catalyst (2.0 wt.% Pd) showed very similar light-off behavior in CO oxidation under lean conditions, with T_{50} values of 83 and 85 °C, respectively [55]. The turnover frequency (TOF) is therefore inferred to be much higher for the perovskite than for dispersed Pd/Al_2O_3, since the fraction of Pd at the surface of the former is necessarily much lower.

In this work, turnover frequencies (TOF) were compared under near-stoichiometric reaction conditions (4.4 Torr CO, 2.3 Torr O_2, 450 K). A TOF of 0.013 s^{-1} was reported for 0.1 wt.% Pd/γ-Al_2O_3, where the authors assumed 100% dispersion of the Pd because of the very low loading [62]. The TOF for Pd-substituted $BaCeO_3$ is estimated to be 0.15 s^{-1} under the same reaction conditions, based on the number of Pd(II) sites exposed on the perovskite surface (0.037 μmol for a 30 mg catalyst sample, see Supplementary material). The higher reactivity therefore compensates for the lower surface area of the perovskite catalyst. The mechanistic origin of the reactivity difference was investigated by exploring the rate laws for CO oxidation over Ba(Ce,Pd)O_3 under CO-lean, CO-rich, and near-stoichiometric reaction conditions.

3.2. Kinetics of CO oxidation over $BaCe_{0.9}Pd_{0.1}O_{2.9}$

Conventional supported noble metal catalysts show strong CO inhibition during the oxidation of CO. This well-known phenomenon is caused by CO poisoning of the exposed metal surface, which prevents adsorption of O_2 and thereby suppresses the formation of adsorbed atomic oxygen required by the Langmuir–Hinshelwood mechanism. The oxidation of CO over Ba(Ce,Pd)O_3 under CO-lean conditions is similarly first-order in O_2 and negative first-order in CO, Fig. 1. Diffusion limitations were assessed according to the Koros-Nowak criteria [63]. External diffusion was investigated by simultaneously doubling both the volumetric flow rate and the amount of catalyst. No external diffusion limitations were discernable under differential reaction conditions, Fig. 1a. No internal diffusion limitations were expected for Ba(Ce,Pd)O_3, since it is non-porous; consistent with this expectation, there was no effect of varying the grain size (30–60 mesh or 80–100 mesh).

Under CO-rich conditions, the P(CO)-dependence of the rate is quite different. At constant $P(O_2) = 3.8$ Torr and $1 \leqslant P(CO)/P(O_2) \leqslant 10$, the reaction order m in P(CO) is −0.41; as $P(CO)/P(O_2)$ increases, the reaction order changes to 0.00, Fig. 2. The P(CO)-dependence of the CO oxidation rate over 2.0 wt.% Pd/γ-Al_2O_3 is also shown for comparison. Under the same conditions, its reaction order m is −0.84 for $3.8 \leqslant P(CO) \leqslant 182$ Torr, in agreement with a report of negative first-order P(CO) dependence over a similar catalyst [64]. The higher reaction orders for Ba(Ce,Pd)O_3 imply a weaker poisoning effect of CO. A similar result was reported for CO oxidation over Pd/CeO_2, whose reaction order m increased from ca. −1 at low P(CO) to zero at high P(CO) [65]. A CeO_2-mediated reaction mechanism was inferred to dominate under the latter conditions. As a result of the lability of its lattice oxygen, CeO_2 supplies atomic oxygen for the oxidation of CO [27,65], and the resulting vacancies provide additional sites for the activation of O_2(g) [66].

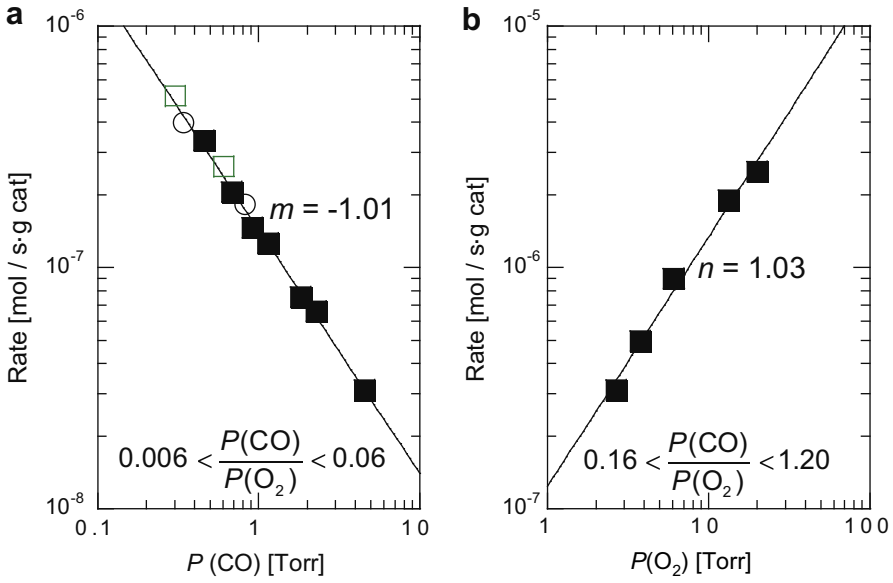

Fig. 1. Dependence of CO oxidation rates over 20 mg catalyst ($BaCe_{0.90}Pd_{0.10}O_{2.90}$, diluted 1:3 w/w in BN, 30–60 mesh) with a total flow rate of 50 mL/min (□), or 40 mg catalyst (30–60 mesh) with a total flow rate of 100 mL/min (■), or 20 mg catalyst (80–100 mesh) with a total flow rate of 50 mL/min (○), under CO-lean conditions at 423 K, on (a) P(CO) at constant $P(O_2) = 76$ Torr; and (b) on $P(O_2)$ at constant P(CO) = 3.2 Torr.

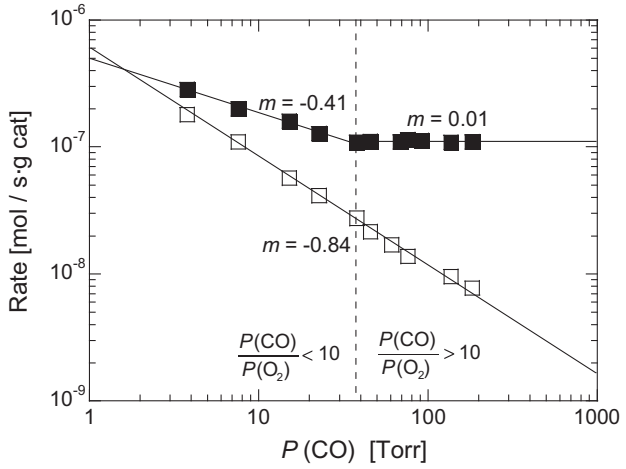

Fig. 2. Dependence of CO oxidation rates over $BaCe_{0.90}Pd_{0.10}O_{2.90}$ (■) and 2 wt.% Pd/Al_2O_3 (□) on P(CO) under CO-rich conditions, at constant $P(O_2)$ = 3.8 Torr and 423 K.

Our previous study [55] demonstrated that the OSC of undoped $BaCeO_3$ is mediocre, but is significantly enhanced when Pd cations are present. No enhancement is observed in the presence of Pd(0). Neutron diffraction studies revealed that oxygen vacancies are created to maintain charge balance when Pd(II) cations occupy *B*-sites of the perovskite lattice, replacing Ce(IV) [54]. The abundance of these vacancies in such complex metal oxides correlates with their fast oxygen mobility [67]. At 423 K and $P(CO)/P(O_2) = 10$, the increase in the apparent order of the reaction in CO from −0.41 to zero suggests a contribution from, and the eventual dominance of, a Mars–van Krevelen mechanism. $BaCeO_3$ plays a role similar to that of CeO_2 itself, whereby CO and O_2 are no longer required to compete for the same adsorption sites. At lower $P(CO)/P(O_2)$, the behavior is intermediate between negative first-order and zero-order in CO (although the non-integer value of m does not have a simple physical meaning under these conditions – see below).

The apparent reaction order n for O_2 under CO-rich conditions varies with P(CO), Fig. 3. For $P(CO) = 3.2$ Torr, n is close to 1; when P(CO) increases to 15.2 Torr, n decreases to 0.49 (similar to Pd/CeO_2, for which $n = 0.44$ was reported under CO-rich conditions [65]). However, the value of n continues to decrease, until it is close to zero at $P(CO) = 91.2$ Torr. The changing apparent reaction order for O_2 confirms that there is another source of atomic oxygen to convert CO into CO_2, viz., the lattice oxygen of Ba(Ce,Pd)O_3. Its participation in the reaction depends on the $P(CO)/P(O_2)$ ratio, accounting for virtually all of the conversion at high $P(CO)/P(O_2)$.

3.3. Rate laws under limiting conditions

For a given set of reaction conditions, the empirical rate law for CO oxidation over Pd-substituted $BaCeO_3$ can be described with the simple power form shown in Eq. (2):

$$rate = k_{obs}P(CO)^m P(O_2)^n \tag{2}$$

where m and n are the apparent reaction orders with respect to CO and O_2, respectively. The kinetics described above show that under CO-lean conditions, only the Langmuir–Hinshelwood mechanism contributes, hence $m = -1$ and $n = +1$. Only the $BaCeO_3$-mediated Mars–van Krevelen mechanism contributes under very CO-rich conditions, with $m = n = 0$. Both mechanisms contribute to the overall reaction under slightly CO-rich conditions ($1 \leqslant P(CO)/P(O_2) \leqslant 10$). In this near-stoichiometric regime, we expect the apparent values of m and n to vary with $P(CO)/P(O_2)$.

The elementary steps for the standard Langmuir–Hinshelwood (LH) mechanism are as follows:

[1] $CO(g) + * \leftrightarrows CO(ad)$ K_1
[2] $O_2(g) + * \rightarrow O_2(ad)$ k_2
[3] $O_2(ad) + * \rightarrow 2O(ad)$
[4] $CO(ad) + O(ad) \rightarrow CO_2(ad) + *$
[5] $CO_2(ad) \leftrightarrows CO_2(g) + *$

where $*$ is a vacant active site (assumed to be a surface Pd site), K_1 is the equilibrium constant for reversible adsorption of CO on this site, and k_2 is the rate coefficient for the non-dissociative adsorption of O_2 on this site. The desorption of O_2 and the recombination of atomic oxygen are assumed to be kinetically insignificant. If step [2] is rate-determining, the rate law for the formation of CO_2 becomes that shown in Eq. (3) [68,69]:

$$rate(LH) = \frac{2k_2P(O_2)}{1 + K_1P(CO)} \approx \frac{2k_2P(O_2)}{K_1P(CO)} \tag{3}$$

where the rate is usually measured per unit weight of catalyst, since the number of active sites is not accurately known. Assuming $K_1 P(CO) \gg 1$, this equation is consistent with the reaction orders observed under CO-lean conditions. (The observed inverse first-order dependence on P(CO) requires that the rate-limiting O_2 adsorption be molecular. A similar conclusion has been reached by others [64,65,69].) However, we note (as have others) [70–72] that the observed kinetics do not exclude an Eley–Rideal mechanism involving the reaction of CO(g) with adsorbed oxygen, which gives rise to the same rate law since the surface reaction (step [4]) is not rate-determining. The Langmuir–Hinshelwood mechanism thus corresponds

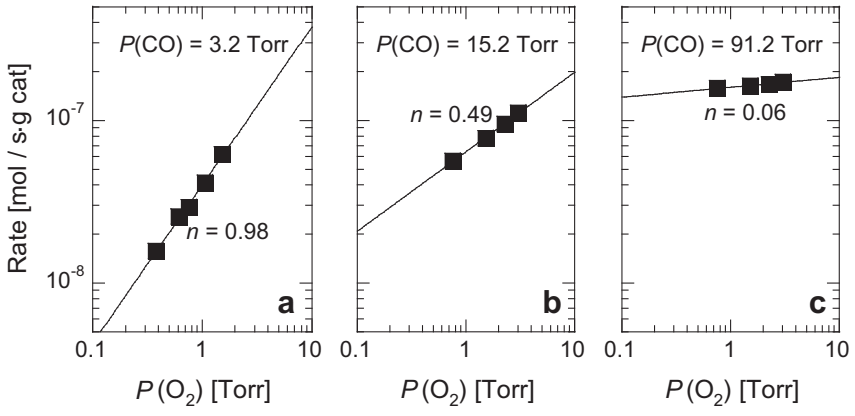

Fig. 3. Dependence of CO oxidation rates over $BaCe_{0.90}Pd_{0.10}O_{2.90}$ on $P(O_2)$, under CO-rich conditions at 423 K, for (a) constant P(CO) = 3.2 Torr; (b) constant P(CO) = 15.2 Torr; and (c) constant P(CO) = 91.2 Torr.

to the "suprafacial" reaction regime (involving adsorbed oxygen) of perovskite-catalyzed oxidations [73].

Under very CO-rich conditions, the reaction orders m and n are both zero, which might suggest that the rate is determined by desorption of CO_2 (step [5]). This was ruled out by the negligible effect on CO conversion of CO_2 (400 ppm) added to the feed (and further confirming that surface $BaCO_3$, if present, does not inhibit the reaction). Alternately, the rate-limiting step may involve intermediates whose concentrations are independent of each other (i.e., they are formed by adsorption on different active sites) and constant (i.e., the active sites are saturated). We propose the following steps corresponding to an "intrafacial" [73], $BaCeO_3$-mediated (BC) oxidation mechanism:

$$[2'] \; O_2(g) + s \rightarrow O_L + O(ad)$$
$$[4'] \; CO(ad) + O_L \rightarrow CO_2(ad) + s \qquad k_{4'}$$

where s is an oxygen vacancy in the perovskite surface. According to this mechanism, Pd^{2+} ions in the $BaCeO_3$ host still serve to adsorb CO(g), step [1]. Step [2′] is analogous to the activation of O_2 over transition metal-doped CeO_2 [31], involving vacancy filling by molecular O_2 and the formation of active oxygen adspecies. However, unlike for Pd/CeO_2 [65], step [2′] cannot be rate-limiting, since the reaction order n varies with $P(CO)/P(O_2)$. It is possible that O_2 adsorbs molecularly on $BaCeO_3$, prior to its dissociation [74]; however, this step is not kinetically observable. The O(ad) species are expected to be highly mobile and to react rapidly with CO(ad) according to step [4].

We note that regeneration of the vacancy (s) requires the removal of lattice oxygen in step [4′]. This appears to be rate-determining, since the resulting rate law is consistent with the absence of any partial pressure dependence, Eq. (4):

$$rate(BC) = 2k_{4'}\theta(CO)\theta(O_L) \approx 2k_{4'} \tag{4}$$

Both $\theta(CO)$, the coverage of CO on accessible, surface Pd sites, and $\theta(O_L)$, the fraction of occupied lattice oxygen sites available for reaction, are essentially unity. The lattice oxygen that participates in the reaction is presumably limited to specific oxygen ions located adjacent to surface Pd sites, but this is not shown explicitly in Eq. (3) since their quantity is not known.

3.4. Rate law under near-stoichiometric reaction conditions

When CO is in slight excess ($1 \leqslant P(CO)/P(O_2) \leqslant 10$), the observed reaction orders are intermediate between those for the Langmuir–Hinshelwood and $BaCeO_3$-mediated mechanisms (e.g., $m = -0.41$ and $n = 0.49$ at 423 K). Under these conditions, the overall rate law includes contributions from both mechanisms, Eq. (5):

$$rate = rate(LH) + rate(BC) = \frac{2k_2P(O_2)}{K_1P(CO)} + 2k_{4'} \tag{5}$$

The same Pd(II) sites serve to adsorb CO in both mechanisms, but the O_2 adsorption sites differ (they are Pd(II) and CeO_2 vacancies for the LH and BC terms, respectively). This relationship illustrates why physically meaningful reaction orders cannot be assigned for either CO or O_2 under near-stoichiometric reaction conditions, a point also made by Nibbelke et al. for CO oxidation over $Pt/Rh/CeO_2/\gamma\text{-}Al_2O_3$ [69]. The non-linear curvefits of this expression to the observed rates are shown in Fig. 4. The temperature-dependent fitted values for k_2/K_1 and $k_{4'}$ are given in Table 1.

3.5. Temperature effects

Under CO-lean conditions at fixed $P(O_2) = 76$ Torr, the value of the apparent reaction order m is −1.0 at 373, 423, and 473 K,

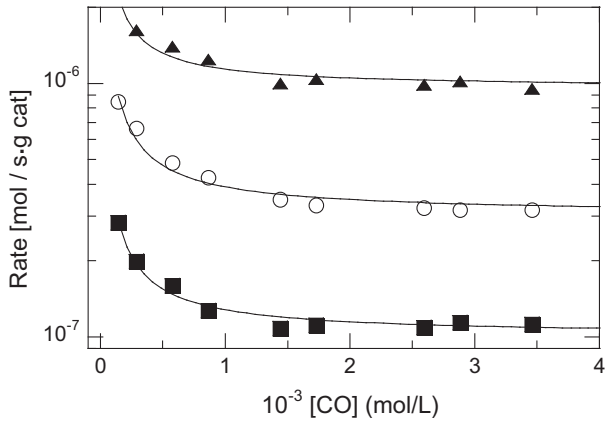

Fig. 4. Curvefit to Eq. (5) of $P(CO)$-dependent oxidation rates over $BaCe_{0.90}Pd_{0.10}O_{2.90}$ under near-stoichiometric conditions, at constant $P(O_2) = 3.8$ Torr and (■) 423 K; (○) 473 K; (▲) 523 K.

Fig. 5a. Thus, the Langmuir–Hinshelwood mechanism dominates over the entire temperature range under these conditions. Under

Table 1
Kinetics parameters for CO oxidation over $BaCe_{0.90}Pd_{0.10}O_{2.90}$ measured under near-stoichiometric reaction conditions.

Temperature (K)	$10^5\ k_2/K_1$ (mol/s g_{cat})	$10^5\ k_{4'}$ (mol/s g_{cat})
423	1.42 ± 0.07	0.82 ± 0.03
473	4.64 ± 0.28	2.44 ± 0.10
523	9.76 ± 0.55	7.68 ± 0.21

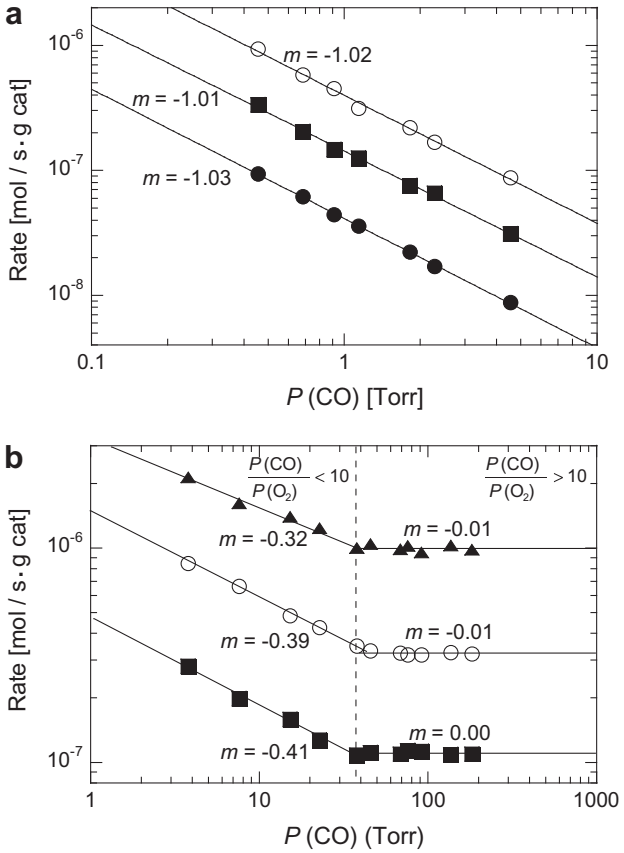

Fig. 5. Rates of CO oxidation over $BaCe_{0.90}Pd_{0.10}O_{2.90}$, with (a) 76 Torr O_2, measured at 373 K (●), 423 K (■), and 473 K (○) and (b) 3.8 Torr O_2, measured at 423 K (■), 473 K (○), and 523 K (▲).

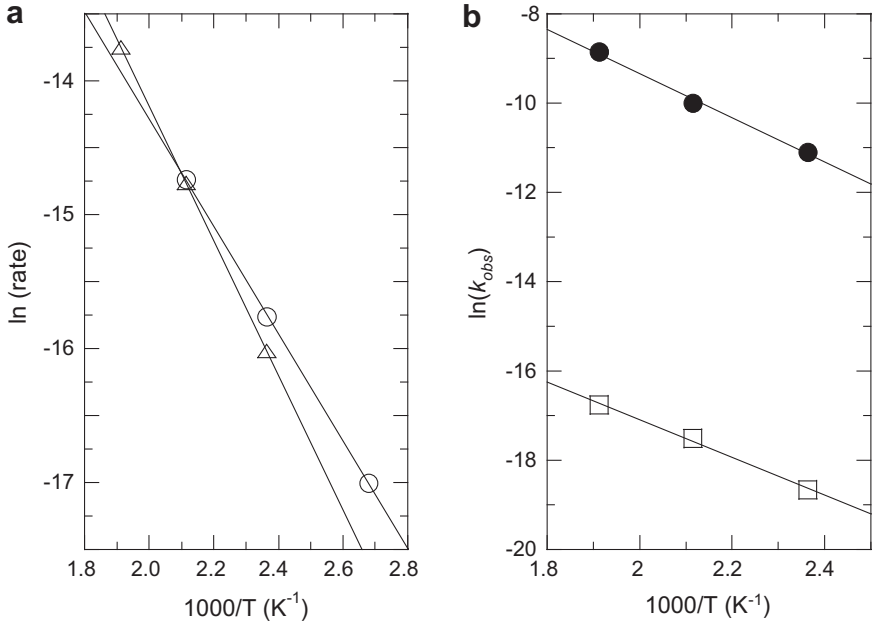

Fig. 6. Arrhenius plots for CO oxidation over $BaCe_{0.90}Pd_{0.10}O_{2.90}$, (a) based on measured rates under CO-rich conditions (38–182.4 Torr CO, 3.8 Torr O_2, Δ) and CO-lean conditions (2.66–20 Torr O_2, 76 Torr CO, ○) and (b) under near-stoichiometric conditions (3.8–38 Torr CO, 3.8 Torr O_2), based on the temperature dependence of ln (k_2/K_1) (□) and ln ($k_{4'}$) (●).

CO-rich conditions, at fixed $P(O_2)$ = 3.8 Torr and $P(CO)/P(O_2) > 10$, there is no $P(CO)$ dependence of the rate from 423 to 523 K, confirming that the $BaCeO_3$-mediated mechanism dominates under these conditions, Fig. 5b. However, for $1 \leqslant P(CO)/P(O_2) \leqslant 10$, the apparent value of m decreases as the temperature increases, from −0.41 at 423 K to −0.32 at 523 K. This trend implies that the contribution of the $BaCeO_3$-mediated mechanism increases with temperature when the feed is close to stoichiometric.

Arrhenius plots for the two limiting reactivity regimes are shown in Fig. 6a. For CO-lean conditions, the activation energy for the Langmuir–Hinshelwood mechanism was obtained directly, $E_{a,LH}$ = (7.8 ± 0.3) kcal/mol. The activation energy for the $BaCeO_3$-mediated mechanism, $E_{a,BC}$, from the temperature dependence of the rate under CO-rich conditions, is (9.7 ± 0.3) kcal/mol. As expected, the apparent activation energy when the reaction conditions are near-stoichiometric, (8.6 ± 0.3) kcal/mol, is intermediate. Although the corresponding Arrhenius plot appears linear (not shown), the fractional contribution of each mechanism, and consequently the apparent activation energy, is temperature-dependent. The approximately linear Arrhenius behavior is due to the similarity of $E_{a,LH}$ and $E_{a,BC}$.

Arrhenius plots for near-stoichiometric conditions can also be constructed using the temperature-dependent kinetic parameters, k_2/K_1 (for LH) and $k_{4'}$ (for BC). The results are shown in Fig. 6b. The resulting activation energies, $E'_{a,BC}$ = (9.7 ± 0.5) kcal/mol and $E'_{a,LH}$ = (8.5 ± 0.5) kcal/mol, agree with those measured under limiting reaction conditions within the stated errors.

The apparent activation energy for CO oxidation by the Langmuir–Hinshelwood mechanism over Pd-substituted $BaCeO_3$, (7.8 ± 0.3) kcal/mol, is much lower than that reported for CO oxidation over Pd/Al_2O_3 (32 kcal/mol) [65]. In both cases, the barrier $E_{a,LH}$ comprises both the barrier for O_2 adsorption ($E_{a,[2]}$) and the CO desorption energy $-\Delta E_{[1]}$, approximated as Eq. (6)

$$E_{a,LH} = E_{a,[2]} - \Delta E_{[1]} \quad (6)$$

where for simplicity, the coverage dependence of the desorption energy has been neglected. For metallic catalysts, the second term dominates and the activation energy is close to the CO desorption energy. The heat of adsorption of CO on Pd(0) (both as single crystals and supported nanoparticles) varies from 22 to 37 kcal/mol, depending on the adsorption site and the CO coverage [75]. The binding energy for CO on Pd(II) (e.g., surface sites in $BaCe_{0.9}Pd_{0.1}O_{2.9}$) may be much lower, due to reduced π-back-donation from the highly ionic metal site [76,77]. The large difference in $E_{a,LH}$ for these two catalysts, despite identical rate laws, is consistent with the active sites on the surface of $BaCe_{0.9}Pd_{0.1}O_{2.9}$ under CO-lean conditions being Pd(II) rather than Pd(0). The much smaller value of $E_{a,LH}$ for $BaCe_{0.9}Pd_{0.1}O_{2.9}$ implies that it is dominated by the first term in Eq (6).

The addition of ceria to Pd/Al_2O_3 was reported to result in a large decrease in the activation barrier for CO oxidation, from 26 to 13 kcal/mol at high $P(CO)$ [65]. In contrast, the activation barrier for the $BaCeO_3$-mediated mechanism described here is slightly higher than the barrier for the Langmuir–Hinshelwood mechanism over Pd-substituted $BaCeO_3$. However, at 9.7 kcal/mol, the barrier for the $BaCeO_3$-mediated mechanism is still lower than the barrier for the CeO_2-mediated mechanism. This may be related to differences in their rate laws (see above). Since $E_{a,BC}$ is the barrier for the elementary step [4′], it is interesting to compare it to the oxygen migration barrier in undoped $BaCeO_3$, 20 kcal/mol [78]. Substitution of a dopant such as Pd(II) into the perovskite creates distortions in the lattice and introduces permanent oxygen vacancies, both of which are expected to facilitate oxygen migration [79,80].

3.6. Local structure of Pd(II) substituted into $BaCeO_3$

Our kinetics results imply that the mechanism for $BaCeO_3$-mediated oxidation involves the participation of lattice oxygen and the transient creation of oxygen vacancies. Since the replacement of Ce(IV) by Pd(II) also requires the formation of permanent oxygen vacancies by removal of a corresponding number of O^{2-} ions for charge neutrality, we investigated the effect of the latter vacancies on the local Pd environment using X-ray absorption spectroscopy (XAS) at the Pd K-edge. The XANES region is shown for $BaCe_{0.93}P$-

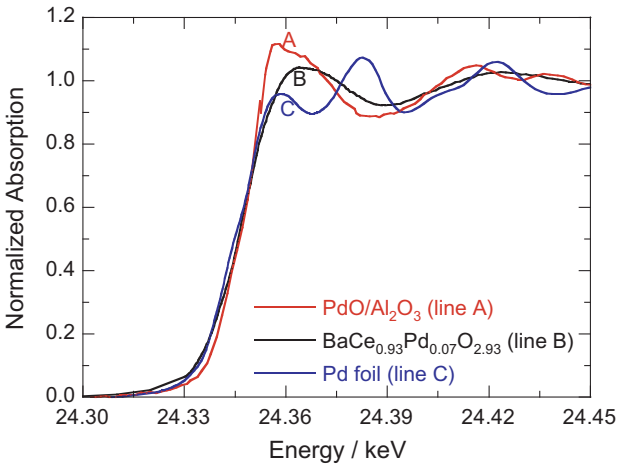

Fig. 7. Comparison of the normalized XANES of $BaCe_{0.93}Pd_{0.07}O_{2.93}$ at the Pd *K*-edge, with the XANES of nanoparticulate $PdO/\gamma\text{-}Al_2O_3$ and Pd foil.

$d_{0.07}O_{2.93}$ in Fig. 7. The Pd environment in the perovskite is clearly different from that of either Pd or PdO.

In order to extract detailed structural information, the EXAFS was analyzed quantitatively. The signal quality is high; the EXAFS region provides usable data up to 16 $Å^{-1}$ in *k*-space and from 1 to 5 Å in *R*-space, Fig. 8. Our FEFF model is based on the results of a recent DFT study [55], which predicted PdO_4 square-planes adjacent to tilted CeO_5 square pyramids and intervening oxygen vacancies, Fig. 9. The curvefit to this model is shown in Fig. 8, with fit parameters given in Table 2. The nearest neighbors consist of a shell of four oxygens at 2.02 Å corresponding to oxygen atoms directly bonded to Pd in square-planar PdO_4. There is also a much longer (weakly-bonded) Pd···O interaction at 2.72 Å.

In the region from 3.0 to 4.5 Å, we expect eight inequivalent Pd–Ba paths and six inequivalent Pd–Ce paths. These were not refined independently, due to the large number of parameters required, but were grouped into a smaller number of similar paths. In particular, tilting of the CeO_5 square pyramid to accommodate square-planar Pd(II) generates three types of Pd–Ce paths: four in the

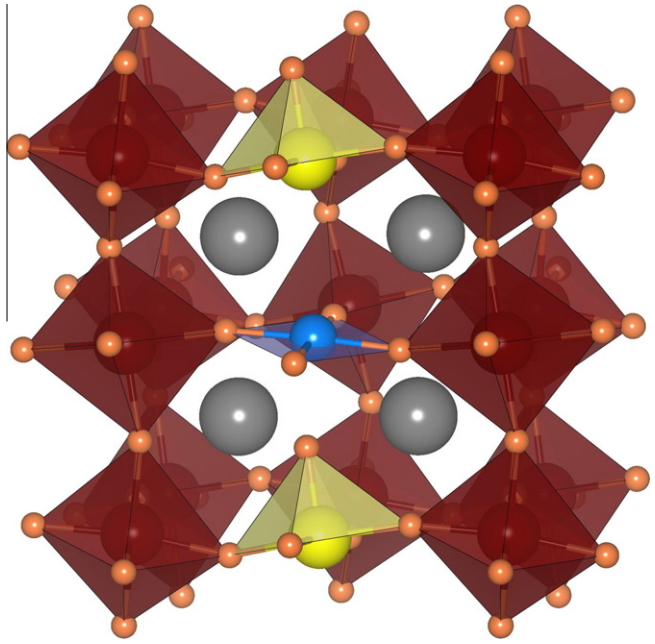

Fig. 9. DFT-calculated [55] bulk structure of $BaCe_{0.875}Pd_{0.125}O_{2.875}$, with an oxygen vacancy between Ce^{4+} and Pd^{2+}, creating CeO_5 square pyramids (yellow). Ba^{2+} is shown in dark grey, O^{2-} in orange, and Pd^{2+} in blue. CeO_6 octahedra are displayed in bordeaux. (For interpretation of the references to colour in this figure legend, the reader is referred to the web version of this article.)

PdO_4 plane, one perpendicular to the PdO_4 plane across the oxygen vacancy, and one perpendicular to the PdO_4 plane across the long Pd···O path. In addition, there are several linear (focused) multiple-scattering paths. Pd–O1–Ce1, Pd–O2–Ce2, and Pd–O1–Ce1–O1 were all predicted to have significant intensity by FEFF and were included in the fit. There is no Pd–O–Ce3 path because of the oxygen vacancy. The triple-scattering Pd–O2–Ce2–O2 path was neglected because of its very low FEFF-predicted amplitude.

Fig. 8 shows the agreement between the EXAFS data and the curvefit. All features between 1 and 5 Å in *R*-space are adequately

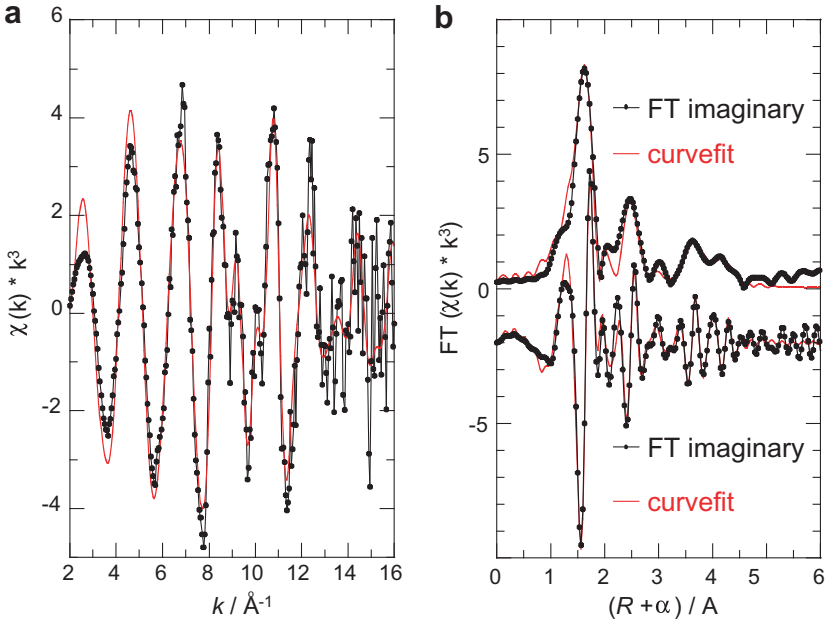

Fig. 8. Pd *K*-edge EXAFS for $BaCe_{0.93}Pd_{0.07}O_{2.93}$, in (a) k^3-weighted *k*-space and (b) *R*-space (not phase-corrected). Curvefit parameters are in Table 2.

Table 2
Curvefit parameters[a] for refinement of the Pd *K*-edge EXAFS of $BaCe_{0.93}Pd_{0.07}O_{2.93}$.

Path	N[b]	d (calc) [55] (Å)	R (Å)	σ^2 (Å^2)
Pd–O1	4	2.04	2.02 (0.00)	0.0038 (0.0003)
Pd···O2	1	2.66	2.72 (0.01)	0.0056 (0.0005)
Pd–Ba1	5	3.58	3.77 (0.02)	0.020 (0.004)
Pd–Ba2	3	3.80	4.04 (0.02)	0.0078 (0.0013)
Pd–Ce1	4	4.38	4.34 (0.09)	0.013 (0.004)[c]
Pd–Ce2	1	4.41	4.38 (0.08)	0.0030 (0.0007)[d]
Pd–Ce3	1	4.65	4.65 (0.04)	0.0017 (0.0006)
Pd–O1–Ce1	8	4.40	4.48 (0.08)	0.013 (0.004)[c]
Pd–O2–Ce2	2	4.69	4.72 (0.07)	0.0030 (0.0007)[d]
Pd–O1–Ce1–O1	4	4.40	4.63 (0.06)	0.013 (0.004)[c]

[a] The value of S_0^2, 0.88, was fixed at the fitted value for *fcc*-Pd. The value of ΔE_0, (5.8 ± 0.9) eV, was refined as a global parameter in the fit. Values in parentheses are the standard deviations of the fitted parameters. The number of independent parameters allowed by the Nyquist criterion [30] is 34 (Δk = 14 Å^{-1}; ΔR = 3.8 Å); the actual number used here is 18. The *R*-factor for this fit is 0.069.

[b] Coordination numbers were fixed at the integer values shown.

[c] The fitted σ^2 values for all collinear paths (single-, double- and triple-scattering) involving Ce1 were constrained together [83].

[d] The fitted σ^2 values for both collinear paths involving Ce2 were constrained together [83].

reproduced, with fit parameters that are reasonable, Table 2. The only σ^2 value that is rather too large is associated with the Pd–Ba1 path; it includes Pd–Ba distances from 3.6 to 3.8 Å in the DFT model. In contrast, the fit to a model containing octahedral Pd(IV) sites is poor especially in the first coordination sphere (see Fig. S2 in Supplementary material). Consequently, the EXAFS supports the computational prediction of square-planar Pd(II) ions with adjacent oxygen vacancies in the bulk.

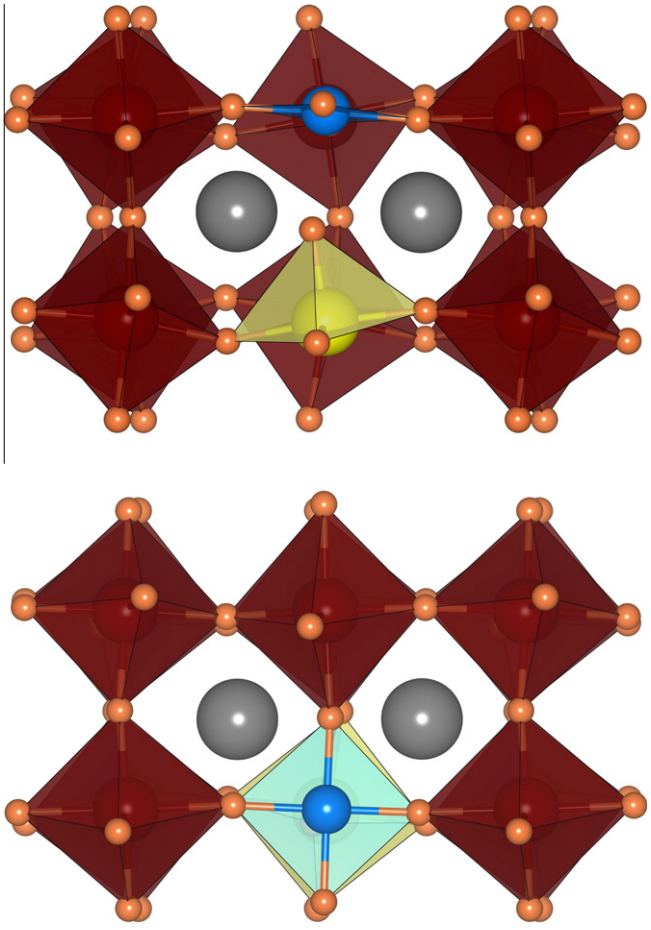

Fig. 10. Simulated surface structure of $BaCe_{0.875}Pd_{0.125}O_{2.875}$ obtained by truncating the bulk structure [55], with an oxygen vacancy above Pd^{2+}, and a CeO_5 square pyramid below. Top: side view; bottom: top view. Ba^{2+} is shown in dark grey, O^{2-} in orange, and Pd^{2+} in blue. CeO_6 octahedra are displayed in bordeaux. (For interpretation of the references to colour in this figure legend, the reader is referred to the web version of this article.)

3.7. Proposed surface structure

On the surface of the Pd-substituted perovskite, the vacancy may be manifested as an open axial coordination site, available for binding reactants, above the PdO_4 plane. This is shown in Fig. 10. Such sites could be created by simple truncation of the bulk structure, although it is also possible that the surface reconstructs [81,82]. In the presence of excess O_2, the oxygen lattice sites are fully populated at the surface, therefore O_2 must compete with CO to bind at the Pd(II) sites. Under CO-rich conditions, the redox flexibility of the Ce^{4+}/Ce^{3+} couple allows the removal of lattice oxygen to create additional oxygen vacancies at the surface. Oxygen adsorption should occur readily at such vacancies, avoiding competition with CO adsorption and forming mobile oxygen adspecies that rapidly oxidize chemisorbed CO. Surface oxygen vacancies may also be filled by oxygen from the bulk, whose mobility is facilitated by the permanent oxygen vacancies created by the substitution of Pd(II) on the Ce(IV) sites. This should allow for the participation of a large fraction of the lattice oxygen in the surface reaction.

4. Conclusions

Despite its low surface area and lack of porosity, crystalline $Ba(Ce,Pd)O_3$ is competent for CO oxidation in both lean and rich reaction conditions. However, the mechanism of CO oxidation changes as a function of $P(CO)/P(O_2)$. Strong CO inhibition in the presence of excess O_2, when the oxygen sublattice of the $BaCeO_3$ surface is highly occupied, demonstrates that CO and O_2 compete for the same adsorption sites, which are assumed to be exposed Pd(II) cations. The lower activation energy of the Langmuir–Hinshelwood mechanism for Pd-doped $BaCeO_3$ relative to Pd/γ-Al_2O_3 is ascribed to the lower CO binding energy on Pd(II) compared to Pd(0). When CO is present in excess, oxygen vacancies are created in the $BaCeO_3$ surface, allowing O_2 activation to occur independent of CO adsorption. At high $P(CO)/P(O_2)$, this $BaCeO_3$-mediated mechanism dominates the kinetics. Under near-stoichiometric reaction conditions, both mechanisms contribute significantly. Since the activation barrier for the $BaCeO_3$-mediated mechanism is slightly higher than for the Langmuir–Hinshelwood mechanism, its contribution increases with temperature.

The similarity of the $BaCeO_3$-mediated mechanism to a previously reported CeO_2-mediated mechanism leads us to propose that the perovskite be considered a BaO-stabilized form of CeO_2. Pd(II) cations are present in the bulk of the $BaCeO_3$ host as PdO_4 square-planes, separated from an adjacent, tilted CeO_5 square pyramid by an oxygen vacancy. The abundance of these oxygen vacancies probably enhances oxygen mobility in the perovskite. High oxygen mobility compensates for the low number of surface adsorption sites. The high thermal stability of the perovskite is potentially advantageous because of the demanding thermal transients experienced by automotive emissions catalysts. The three-way activity and sulfur tolerance of Pd-substituted $BaCeO_3$ are under investigation.

Acknowledgments

The authors thank Dr. Jun Li for providing samples of Pd-substituted $BaCeO_3$, Prof. Ram Seshadri and Brian Vicente for helpful discussions. X.O. is grateful to Air Products for a Graduate Fellowship.

The authors acknowledge financial support by the US Department of Energy, Office of Basic Energy Sciences, Catalysis Science Grant No. DE-FG02-03ER15467. Portions of this research were carried out at the Stanford Synchrotron Radiation Lightsource, a national user facility operated by Stanford University on behalf of the US Department of Energy, Office of Basic Energy Sciences.

Appendix A. Supplementary material

Supplementary data associated with this article can be found, in the online version, at doi:10.1016/j.jcat.2010.04.020.

References

[1] J. Kaspar, P. Fornasiero, M. Graziani, Catal. Today 50 (1999) 285.
[2] T. Miki, T. Ogawa, M. Haneda, N. Kakuta, A. Ueno, S. Tateishi, S. Matsuura, M. Sato, J. Phys. Chem. 94 (1990) 6464.
[3] P. Fornasiero, R. Dimonte, G.R. Rao, J. Kaspar, S. Meriani, A. Trovarelli, M. Graziani, J. Catal. 151 (1995) 168.
[4] A. Trovarelli, Catal. Rev. Sci. Eng. 38 (1996) 439.
[5] C.E. Hori, H. Permana, K.Y.S. Ng, A. Brenner, K. More, K.M. Rahmoeller, D. Belton, Appl. Catal. B: Environ. 16 (1998) 105.
[6] W.J. Stark, M. Maciejewski, L. Madler, S.E. Pratsinis, A. Baiker, J. Catal. 220 (2003) 35.
[7] K. Krishna, A. Bueno-Lopez, M. Makkee, J.A. Moulijn, Appl. Catal. B: Environ. 75 (2007) 189.
[8] K. Krishna, A. Bueno-Lopez, M. Makkee, J.A. Moulijn, Appl. Catal. B: Environ. 75 (2007) 201.
[9] K. Krishna, A. Bueno-Lopez, M. Makkee, J.A. Moulijn, Appl. Catal. B: Environ. 75 (2007) 210.
[10] M. Machida, Y. Murata, K. Kishikawa, D. Zhang, K. Ikeue, Chem. Mater. 20 (2008) 4489.
[11] S. Rossignol, Y. Madier, D. Duprez, Catal. Today 50 (1999) 261.
[12] J.A. Montoya, E. Romero-Pascual, C. Gimon, P. Del Angel, A. Monzon, Catal. Today 63 (2000) 71.
[13] Y. Zhang, S. Andersson, M. Muhammed, Appl. Catal. B: Environ. 6 (1995) 325.
[14] K. Higashi, K. Sonoda, H. Ono, S. Sameshima, Y. Hirata, J. Mater. Res. 14 (1999) 957.
[15] R. Strobel, A. Baiker, S.E. Pratsinis, Adv. Powder Technol. 17 (2006) 457.
[16] R. Kydd, W.Y. Teoh, K. Wong, Y. Wang, J. Scott, Q.H. Zeng, A.B. Yu, J. Zou, R. Amal, Adv. Funct. Mater. 19 (2009) 369.
[17] X.H. Yu, F. Li, X.R. Ye, X.Q. Xin, Z.L. Xue, J. Am. Ceram. Soc. 83 (2000) 964.
[18] F. Li, X.H. Yu, H.J. Pan, M.L. Wang, X.Q. Xin, Solid State Sci. 2 (2000) 767.
[19] A. Mukherjee, D. Harrison, E.J. Podlaha, Electrochem. Solid-State Lett. 4 (2001) D5.
[20] R. Inguanta, S. Piazza, C. Sunseri, Nanotechnology 18 (2007) 485605.
[21] A. Trovarelli, G. Dolcetti, C. Deleitenburg, J. Kaspar, P. Finetti, A. Santoni, J. Chem. Soc., Faraday Trans. 88 (1992) 1311.
[22] C. Deleitenburg, A. Trovarelli, J. Catal. 156 (1995) 171.
[23] S. Bernal, J.J. Calvino, M.A. Cauqui, J.M. Gatica, C. Larese, J.A.P. Omil, J.M. Pintado, Catal. Today 50 (1999) 175.
[24] S. Penner, D. Wang, R. Podloucky, R. Schlogl, K. Hayek, Phys. Chem. Chem. Phys. 6 (2004) 5244.
[25] M. Fuchs, B. Jenewein, S. Penner, K. Hayek, G. Rupprechter, D. Wang, R. Schlogl, J.J. Calvino, S. Bernal, Appl. Catal. A: Gen. 294 (2005) 279.
[26] C.M.Y. Yeung, S.C. Tsang, J. Phys. Chem. C 113 (2009) 6074.
[27] T. Bunluesin, H. Cordatos, R.J. Gorte, J. Catal. 157 (1995) 222.
[28] H. He, H.X. Dai, L.H. Ng, K.W. Wong, C.T. Au, J. Catal. 206 (2002) 1.
[29] Y. Madier, C. Descorme, A.M. Le Govic, D. Duprez, J. Phys. Chem. B 103 (1999) 10999.
[30] T. Baidya, A. Gupta, P.A. Deshpandey, G. Madras, M.S. Hegde, J. Phys. Chem. C 113 (2009) 4059.
[31] M.F. Camellone, S. Fabris, J. Am. Chem. Soc. 131 (2009) 10473.
[32] Q. Liang, X. Wu, D. Weng, H. Xu, Catal. Today 139 (2008) 113.
[33] M. Machida, Y. Murata, K. Kishikawa, D.J. Zhang, K. Ikeue, Chem. Mater. 20 (2008) 4489.
[34] K.Z. Li, H. Wang, Y.G. Wei, D.X. Yan, J. Phys. Chem. C 113 (2009) 15288.
[35] R.A. Dalla Betta, T. Rostrup-Nielsen, Catal. Today 47 (1999) 369.
[36] S.J. Schmieg, D.N. Belton, Appl. Catal. B: Environ. 6 (1995) 127.
[37] J. Fan, X.D. Wu, Q. Liang, R. Ran, D. Weng, Appl. Catal. B: Environ. 81 (2008) 38.
[38] Y. Nagai, K. Dohmae, Y. Ikeda, N. Takagi, T. Tanabe, N. Hara, G. Guilera, S. Pascarelli, M.A. Newton, O. Kuno, H.Y. Jiang, H. Shinjoh, S. Matsumoto, Angew. Chem. Int. Ed. 47 (2008) 9303.
[39] Y. Nishihata, J. Mizuki, T. Akao, H. Tanaka, M. Uenishi, M. Kimura, T. Okamoto, N. Hamada, Nature 418 (2002) 164.
[40] N. Minkova, S. Aslanian, Cryst. Res. Technol. 24 (1989) 351.
[41] H.T. Anderson, B.J. Wuensch, J. Am. Ceram. Soc. 56 (1973) 285.
[42] A. Piras, A. Trovarelli, G. Dolcetti, Appl. Catal. B: Environ. 28 (2000) L77.
[43] E. Rocchini, A. Trovarelli, J. Llorca, G.W. Graham, W.H. Weber, M. Maciejewski, A. Baiker, J. Catal. 194 (2000) 461.
[44] T. Luo, R.J. Gorte, Catal. Lett. 85 (2003) 139.
[45] T. Luo, R.J. Gorte, Appl. Catal. B: Environ. 53 (2004) 77.
[46] L. Limousy, H. Mahzoul, J.F. Brilhac, P. Gilot, F. Garin, G. Maire, Appl. Catal. B: Environ. 42 (2003) 237.
[47] E. Fridell, M. Skoglundh, B. Westerberg, S. Johansson, G. Smedler, J. Catal. 183 (1999) 196.
[48] F. Prinetto, G. Ghiotti, I. Nova, L. Lietti, E. Tronconi, P. Forzatti, J. Phys. Chem. B 105 (2001) 12732.
[49] L.F. Liotta, G. Pantaleo, A. Macaluso, G. Di Carlo, G. Deganello, Appl. Catal. A: Gen. 245 (2003) 167.
[50] H. Iwahara, H. Uchida, K. Ono, K. Ogaki, J. Electrochem. Soc. 135 (1988) 529.
[51] F. Giannici, A. Longo, A. Balerna, A. Martorana, Chem. Mater. 21 (2009) 597.
[52] A. Cammarata, A. Martorana, D. Duca, J. Phys. Chem. A 113 (2009) 6381.
[53] J.E. Miller, A.G. Sault, D.E. Trudell, T.M. Nenoff, S.G. Thoma, N.B. Jackson, Appl. Catal. A: Gen. 201 (2000) 45.
[54] J. Li, U.G. Singh, J.W. Bennett, K. Page, J.C. Weaver, J.P. Zhang, T. Proffen, A.M. Rappe, S. Scott, R. Seshadri, Chem. Mater. 19 (2007) 1418.
[55] U.G. Singh, J. Li, J.W. Bennett, A.M. Rappe, R. Seshadri, S.L. Scott, J. Catal. 249 (2007) 349.
[56] A. Steigel, J. Sauer, D.A. Kleier, G. Binsch, J. Am. Chem. Soc. 94 (1972) 2770.
[57] M. Newville, J. Synchrotron Rad. 8 (2001) 322.
[58] S.I. Zabinsky, J.J. Rehr, A. Ankudinov, R.C. Albers, M.J. Eller, Phys. Rev. B 52 (1995) 2995.
[59] W.C. Wang, Y. Chen, Phys. Status Solidi A 168 (1998) 351.
[60] B. Ravel, M. Newville, J. Synchrotron Rad. 12 (2005) 537.
[61] C.N. Rao, K.K. Rao, Can. J. Phys. 42 (1964) 1336.
[62] D.R. Rainer, M. Koranne, S.M. Vesecky, D.W. Goodman, J. Phys. Chem. B 101 (1997) 10769.
[63] M. Boudart, G. Djéga-Mariadassou, Kinetics of Heterogeneous Catalytic Reactions, Princeton Univ. Press, Princeton, NJ, 1984.
[64] J. Rodriguez, D. Wayne Goodman, Surf. Sci. Rep. 14 (1991) 1.
[65] T. Bunluesin, E.S. Putna, R.J. Gorte, Catal. Lett. 41 (1996) 1.
[66] T. Bunluesin, R.J. Gorte, G.W. Graham, Appl. Catal. B: Environ. 14 (1997) 105.
[67] J.A. Kilner, Solid State Ionics 129 (2000) 13.
[68] R. Sant, E.E. Wolf, Chem. Eng. Sci. 45 (1990) 3137.
[69] R.H. Nibbelke, M.A.J. Campman, J. Hoebink, G.B. Marin, J. Catal. 171 (1997) 358.
[70] H.P. Bonzel, R. Ku, J. Vac. Sci. Technol. 9 (1972) 663.
[71] C.H.F. Peden, D.W. Goodman, M.D. Weisel, F.M. Hoffmann, Surf. Sci. 253 (1991) 44.
[72] A. Bottcher, H. Niehus, S. Schwegmann, H. Over, G. Ertl, J. Phys. Chem. B 101 (1997) 11185.
[73] R.J.H. Verhooeve, Advanced Materials in Catalysis, Academic, New York, 1977.
[74] C. Li, K. Domen, K. Maruya, T. Onishi, J. Am. Chem. Soc. 111 (1989) 7683.
[75] E.H. Voogt, L. Coulier, O.L.J. Gijzeman, J.W. Geus, J. Catal. 169 (1997) 359.
[76] B. Kalita, R.C. Deka, Eur. Phys. J. D 53 (2009) 51.
[77] D.B. Dell'Amico, L. Labella, F. Marchetti, S. Samaritani, Coord. Chem. Rev. 254 (2010) 635.
[78] R. Glockner, M.S. Islam, T. Norby, Solid State Ionics 122 (1999) 145.
[79] J.A. Kilner, R.J. Brook, Solid State Ionics 6 (1982) 237.
[80] M. Cherry, M.S. Islam, C.R.A. Catlow, J. Solid State Chem. 118 (1995) 125.
[81] S. Colussi, A. Gayen, M.F. Camellone, M. Boaro, J. Llorca, S. Fabris, A. Trovarelli, Angew. Chem. Int. Ed. 48 (2009) 8481.
[82] F. Cora, C.R.A. Catlow, Faraday Discuss. 114 (1999) 421.
[83] P. Shanthakumar, M. Balasubramanian, D.M. Pease, A.I. Frenkel, D.M. Potrepka, V. Kraizman, J.I. Budnick, W.A. Hines, Phys. Rev. B 74 (2006) 174103.